remote sensing

MDPI

Article

Mineral Exploration Potential Estimation Using 3D Inversion: A Comparison of Three Different Norms

Tao Chen [1,2] and Guibin Zhang [1,*]

[1] School of Geophysics and Information Technology, China University of Geosciences, Beijing 100083, China; chent7@sustech.edu.cn or chentaosx@hotmail.com
[2] Department of Earth and Space Sciences, Southern University of Science and Technology, Shenzhen 518055, China
* Correspondence: gbzhang@cugb.edu.cn; Tel.: +86-010-82321929

Abstract: Gravity data have been frequently used in researching the subsurface to map the 3D geometry of the density structure, which is considered the basis for further interpretations, such as the estimation of exploration potential in mineral exploration. The gravity inversion, practically employed to map the density structure, can be achieved by different methods. The method based on Tikhonov regularization is the most commonly used among them. Usually, the subsurface is discretized into a set of cells or voxels. To recover a stable and reliable solution, constraints are introduced into the Tikhonov regularization. One constrained inversion introduces a quadratic penalty (L_2 norm) into the inversion, which imposes smooth features on the recovered model. Another gravity inversion, known as sparse inversion, imposes compactness and sharp boundaries on the recovered density structure. Specifically, the L_1 norm and L_0 norm are favored for such a purpose. This work evaluates the merits of the gravity data inversion in cooperation with different model norms and their applicability in exploration potential estimation. Because these norms promote different features in the recovered models, the reconstructed 3D density structure reveals different geometric features of the ore deposit. We use two types of synthetic data for evaluating the performances of the inversion with different norms. Numerical results demonstrate that L_0 norm-based inversion provides high-resolution recovered models and offers reliable estimates of exploration potential with minimal deviation from theoretical mass compared to inversions equipped with the other two norms. Finally, we use the gravity data collected over the iron ore deposit at the Dida mining area in Jilin province (Northeast China) for the application. It is estimated that the exploration potential of the iron ore deposits is about 3.2 million tons.

Keywords: gravity; 3D inversion; exploration potential estimation; L_2 norm; L_1 norm; L_0 norm; Jilin province

Citation: Chen, T.; Zhang, G. Mineral Exploration Potential Estimation Using 3D Inversion: A Comparison of Three Different Norms. *Remote Sens.* **2022**, *14*, 2537. https://doi.org/10.3390/rs14112537

Academic Editors: Cassiani Giorgio, Gian Piero Deidda and Mahjoub Himi

Received: 1 May 2022
Accepted: 23 May 2022
Published: 25 May 2022

1. Introduction

The economic evaluation of a deposit is an essential factor in opening a new mine or planning investments for future mine operations. However, this economic assessment relies on the accuracy of the associated exploration potential estimation. A reliable estimation of exploration potential in tonnage is crucial for the subsequent investment during the exploration phase. Furthermore, the profitability of mining projects usually relies on the quality assessment results obtained during the exploration potential estimation process. Therefore, reliable exploration potential estimates for deposits such as iron ore are critical to successful and profitable mining operations.

Traditionally, geoscientists have utilized geometric and geostatistical methods to evaluate a total mass estimate for the exploration target [1–7]. Specifically, the geometric method, such as the classical polygon method, is usually applied when a sufficiently large database is not available, and it provides a rough estimate of the tonnage of a

mineral deposit [8,9]. The geostatistical method, which models an ore deposit using the spatial distribution of the ore grades, is treated as a more sophisticated method and receiving increasing attention [3,10–12]. However, these two methods rely heavily on the availability of core samples, which can be expensive for large, deep deposits. The accuracy of geostatistical inferences can also vary widely depending on the distribution of core samples and the method used. In general, geometric and geostatistical methods are suitable when the deposit is shallow or sufficient geological information is available.

By contrast, methods based on geophysical inversion offer an alternative. Geophysical inversion converts remotely sensed physical fields into the distribution of physical property. Ore exploration potential can then be estimated from the distribution of certain physical property values that are empirically classified as ore in a particular exploration environment. Exploration potential estimation based on geophysical inversion is highlighted for efficiency and cost-effectiveness. Recently, the authors of [13] used airborne magnetic data to evaluate the iron (magnetite) deposits via 3D inversion equipped with L_2 norm; exploration potential in tonnage was calculated from volume and estimated mean density. Other geophysical surveys can similarly be used for exploration potential estimation. In fact, gravity surveys and the resulting density distribution can be instrumental since tonnage can be directly calculated as the product of the recovered density and the corresponding volume, avoiding conversions between other physical properties and densities.

In terms of gravity inversion, it is an ill-posed optimization problem. The widely applied Tikhonov regularization imposes constraints on the recovered model to stabilize the minimization process. Traditionally, the L_2 norm penalty, known as the smoothness constraint, is introduced to yield a simple, minimum structure that fits the observed data to a reasonable level [14,15]. However, the L_2 model norm-based inversion tends to recover a fuzzy structure because the quadratic model norm penalty introduces a certain degree of smoothness into the inverted structure. These features will be more pronounced if further smoothing constraints on the model (first- or second-order difference operators) are introduced in the objective function. The compact or sparse constraint has attracted increasing attention in mineral surveys because it produces a model of blocky features that facilitates further interpretation and sets the stage for subsequent mineral exploration. Regarding sparse constraints, the L_0 norm is favored, which penalizes the number of non-zero model parameters while ignoring their magnitude [16]. The L_0 norm has been widely used in different fields, including anisotropic point cloud denoising [17], signal recovery [18], image reconstruction [19], face recognition [20], and spectrum reconstruction [21]. The L_0 norm also highlights its position in geophysical data processing and inversion. The author of [22] used the L_0 norm for potential field and seismic data reconstruction. The author of [23] employed the L_0 norm for electrical resistivity tomography and demonstrated its characteristic in imaging small-scale targets with sharp boundaries. In seismic impedance inversion, the L_0 gradient minimization regularization provides a blocky solution that makes the formation interfaces and geological edges more precise and keeps the inversion procedure robust even if random noise exists in the seismic data [24]. The L_0 norm has been further developed in the potential field data inversion. Different approximate expressions for the L_0 norm have been successfully applied in the inversion [25–28], and sharp boundaries feature the inversion results. Alternatives to the L_0 norm penalty, such as the L_1 norm penalty, are also popular in the geophysics community [29,30]. Different norm penalties have advantages and disadvantages in terms of application scenarios, recovery of geometric and physical properties of density structures, time consumption, etc.

Forward modeling is an integral part of inversion. In gravity forward modeling, according to the basic geometric model used, it can be divided into the stack of rectangular prisms [31], the stack of polygonal prisms [32], and the polyhedron [33]. Due to the convenience of discretization and integration, the stack of rectangular prisms is widely used in practice and adopted in our work. The closed-form expressions of the gravity effect due to a rectangular prism have been derived by many researchers [31,34,35]. However,

their differences are slight, and the interested readers are recommended to refer to [36] for a complete comparison of different closed-form expressions.

This paper explores the exploration potential estimation problem using 3D gravity inversion equipped with different norm penalties. Our work builds an objective function that comprises the data misfit, model penalty (L_2 norm, L_1 norm, and L_0 norm), and the bound constraints using a logarithmic barrier term. When minimizing the objective function, the iteratively reweighted least-squares (IRLS) [37] technique is utilized, and the regularization parameter is determined with a line search principle. In the following, we first present the forward modeling and inversion methods involved in this research. Then we test the effectiveness of exploration potential estimation using 3D inversion with different norm penalties based on two synthetic datasets. Finally, gravity data collected from the Dida area in northeast China were used to verify the applicability of various model norms in estimating ore exploration potential in a real mining scenario.

2. Methods

Regarding a real field survey, the estimation of exploration potential comprises three main steps (Figure 1). Firstly, the raw gravity data were processed to obtain residual Bouguer gravity anomalies; these procedures include various corrections, field separation, and denoising. Furthermore, petrophysical information was gathered from the literature and rock sample measurements. Secondly, we adopted different norm-based inversions in cooperating with the petrophysical information to obtain recovered models. Finally, the recovered model was utilized to perform an estimation of the exploration potential. Since gravity data and density distribution correlate directly, the exploration potential was estimated by multiplying the exploration target involved volume and inverted density. In particular, the L_2 norm inverted model had smooth features, so a cutoff process was required to extract the cropped model relevant to the exploration target. The remainder of this section focuses on the inversion method (light blue parts in Figure 1) and presents the details related to the forward modeling and inversion equipped with different norms.

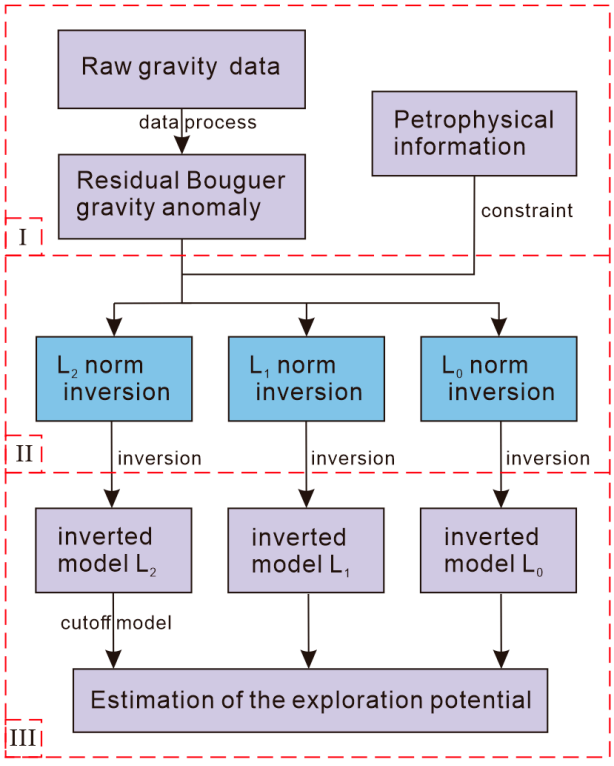

Figure 1. Flowchart of the inversion-based estimation of the exploration potential.

2.1. Closed-Form Solution of Gravity Field

Considering the Cartesian coordinate systems, we adopted the coordinates (x, y, z) for a survey point and (ξ, η, ζ) for a geological body (Figure 2a). The vertical axes (z and ζ), the north axes (x and ξ), and the east axes (y and η) were arranged in a right-handed system. The gravity effect g caused by a rectangular cell with a constant density ρ at survey point (x, y, z) is given by [36]

$$g = -\gamma\rho\sum_{i=1}^{2}\sum_{j=1}^{2}\sum_{k=1}^{2}\mu_{ijk}\times\left[x_i\ln\left(y_j+r_{ijk}\right)+y_j\ln\left(x_i+r_{ijk}\right)+z_k\arctan\frac{z_k r_{ijk}}{x_i y_j}\right], \quad (1)$$

where γ is the universal gravitational constant, $x_i = x—\xi_i$, $y_j = y—\eta_j$, $z_k = z—\zeta_k$, $r_{ijk} = \sqrt{{x_i}^2+{y_j}^2+{z_k}^2}$, and $\mu_{ijk} = (-1)^{i+j+k}$. Coordinates of the rectangular cell are limited by $\xi_1 \le \xi \le \xi_2$, $\eta_1 \le \eta \le \eta_2$, and $\zeta_1 \le \zeta \le \zeta_2$.

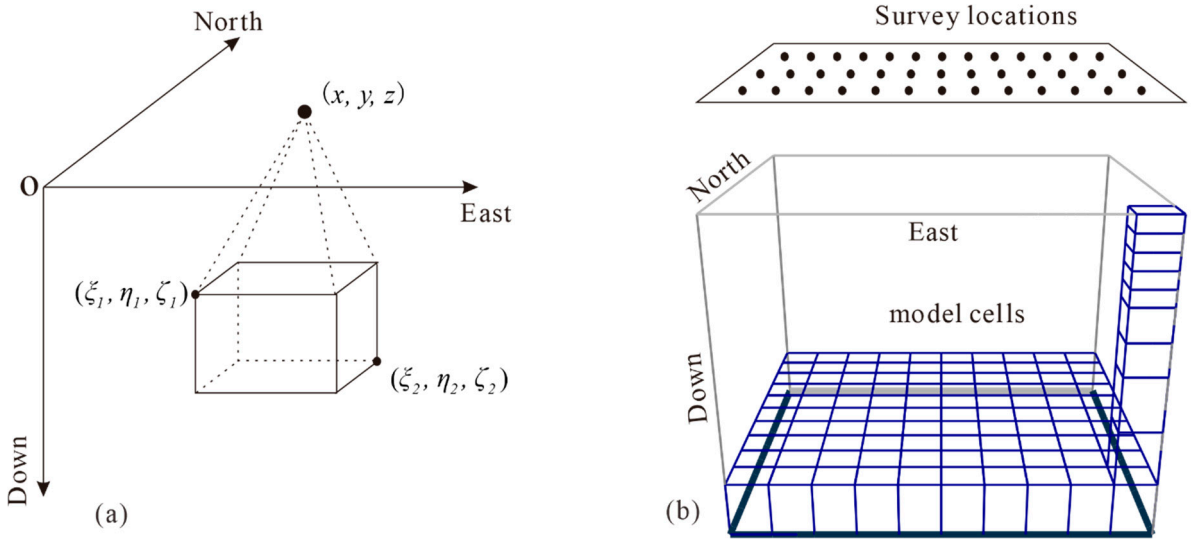

Figure 2. (**a**) Graphical illustration of calculating the gravity effect produced by a model cell with respect to survey point (x, y, z). (**b**) Model cells and survey locations, only part of model cells are shown [38].

The geological body with arbitrary geometry could be approximated using a set of rectangular cells. For each cell, we assumed that its density was a constant. Then, according to the superposition principle, the gravity anomaly of the arbitrary density distribution at survey locations was obtained by summing the contributions from all cells (Figure 2b). The matrix-vector form of the forward modeling can be expressed as:

$$\mathbf{d} = \mathbf{Gm}, \quad (2)$$

where $\mathbf{d}$ is an N-length vector composed of observed data (gravity anomalies in this paper). $\mathbf{m}$ denotes the M-length vector composed of the model parameters (density vector in this paper). $\mathbf{G}$ represents the sensitivity or the Jacobi matrix, with a size of $N \times M$, which characterizes the contribution of changes in model parameters on the observed data.

2.2. Principles of Inversion Approaches

This section presents inversion methods using the different model norm constraints. It is well-known that geophysical data inversion is an ill-posed problem. From the data point of view, measurements were performed at discrete, limited locations, and the measured responses were usually inaccurate. From the model's perspective, the complex subsurface structure increased the ill-posedness of the problem. As a result, the traditional least-squares inversion would most likely produce an unreliable model. The Tikhonov regularization-

based inversion increased the model's reliability by adding constraints to the inverted model and ultimately reducing the interpretation ambiguity. In this work, the Tikhonov regularization was utilized as [39]

$$\phi(\mathbf{m}) = \|\mathbf{W}_d(\mathbf{d} - \mathbf{G}\mathbf{m})\|_2^2 + \mu\|\mathbf{W}_m\mathbf{m}\|_p^p, \tag{3}$$

where $\phi(\mathbf{m})$ denotes the objective function. The first term of the right-hand side (RHS) is called data misfit, which evaluated the fitting error of the inverted model's forward response with respect to the observed data $\mathbf{d}$. The second term of RHS is the model norm, which was introduced to stabilize the minimization process. $\mathbf{W}_d$ is a diagonal data weighting matrix, which provided an estimation of the uncertainty of observed data. $\mathbf{W}_m$ denotes the model weighting matrix, set as the cell volume weighting operator. It was noted that both $\mathbf{G}$ and $\mathbf{m}$ are normalized by a depth weighting matrix to compensate for the decay of the kernel function [15,40]. The μ represents the regularization parameter, balancing the relative importance between the data misfit and the model norm during the inversion process. The choice of μ plays a vital role in the inversion; available options were the L-curve method [41], generalized cross-validation method [42], the cooling method [43], etc. During the iteration, we calculated the μ using the line search strategy to decrease the data misfit. The following equation was used to calculate the initial regularization parameter [43]

$$\mu = \frac{s_{\max}\left(\mathbf{G}^T\mathbf{W}_d^T\mathbf{W}_d\mathbf{G}\right)}{s_{\max}\left(\mathbf{W}_m^T\mathbf{W}_m\right)}, \tag{4}$$

where $s_{\max}$ $(\mathbf{A})$ denotes the largest singular value of the matrix $\mathbf{A}$.

For different p values, the second term on the RHS of Equation (3) varies its form as follows [44,45]

$$\|\mathbf{m}\|_0^0 = \sum_{i=1}^{M} \log(m_i^2 + \varepsilon^2), \tag{5}$$

$$\|\mathbf{m}\|_1^1 = \sum_{i=1}^{M} \left(m_i^2 + \varepsilon^2\right)^{1/2}, \tag{6}$$

$$\|\mathbf{m}\|_2^2 = \sum_{i=1}^{M} m_i^2, \tag{7}$$

where ε is a small number to avoid singularity and is set to 10^{-10}. Figure 3 illustrates the penalties for different norms. Theoretically, the L_2 norm is very sensitive to the amplitude of the model parameter due to squaring. While the L_2 norm is the most common usage, it is mostly blind to geometry and tends to recover model with smaller parameters than the actual case. The L_1 norm inverted model could be interpreted as a minimal geometric description, which is somewhat sensitive to amplitude information. Most of the model parameters restored using the L_1 norm tend to be zero, and a small number of model parameters have high values. However, the boundary of the target was blurred due to the nature of the L_1 norm. The L_0 norm was the least amplitude-dependent norm since it was counted regardless of the magnitude (if the absolute value of a number is raised to the power of 0, then it is 1 or 0). During the minimization, the vast majority of model parameters became 0, and only a few model parameters, used to characterize the geological bodies, had non-zero value and sharp-boundary features [46]. To sum up the above, the inversion equipped with the L_0 norm tended to provide more robust and interpretable results than other norms.

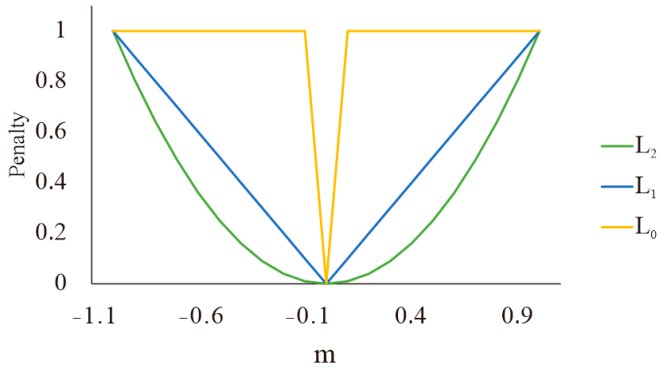

Figure 3. Graphical representation of different norms over the interval [–1, 1].

In the minimization phase, the L_2 norm-based inversion was solved using a classical Gauss-Newton approach [47]. The L_0 and L_1 norm-based inversions were solved as an iteratively reweighted least-squares (IRLS) problem [37]. We refer the reader to [37,44] for detailed explanations. Here, we briefly review the process. In the IRLS framework, the minimization of the L_0 and L_1 model norm-based inversion was equivalent to solving an L_2 norm-based inversion as follows

$$\phi(\mathbf{m}) = \|\mathbf{W}_d(\mathbf{d} - \mathbf{G}\mathbf{m})\|_2^2 + \mu\|\mathbf{W}_n\mathbf{W}_m\mathbf{m}\|_2^2, \tag{8}$$

where $\mathbf{W}_n$ is the diagonal weighting matrix related to the Equations (5) and (6), and its diagonal element has the form of [44]

$$\mathbf{W}_n^{jj} = \left(|m_j|^2 + \varepsilon^2\right)^{\frac{p-2}{4}}, \tag{9}$$

where p equals 0 or 1 according to the model norm, and the m_j represents the model parameter of the jth cell. It was noted that $\mathbf{W}_n$ is a variable weighting operator which depended on the model parameters while $\mathbf{W}_m$ remains unchanged.

2.3. Bound Constraint

During the minimization of Equations (3) and (8), the program searched for the solution in the feasible domains under the model norm constraints. However, the solution could be ambiguous from the perspective of interpretation. One of the reasons is that the recovered model mismatched the petrophysical information from the drill holes or geological mapping. Fortunately, several mathematical techniques were available for adding such a constraint into the recovered model, which substantially reduced the uncertainty of the inversion and improved our confidence in the interpretation. In our implementation, we employed the logarithmic barriers method to impose the bound constraints on the inverted model. Specifically, an additional term was added to the RHS of the Equations (3) and (8), which was expressed as

$$\phi_{bnd}(\mathbf{m}) = -\sum_{i=1}^{M}\left[\log\left(\frac{m_j - m_{\min}}{m_{\max} - m_{\min}}\right) + \log\left(\frac{m_{\max} - m_j}{m_{\max} - m_{\min}}\right)\right] \tag{10}$$

where the $m_{\min}$ and $m_{\max}$ are the model parameters' lower and upper bounds for each cell, respectively.

A practical technique for minimizing Equations (3) or (8) with the constraints of equation (10) was based on the standard IRLS algorithm. Specifically, we first updated the model $\mathbf{m}$ with a fixed $\mathbf{W}_n$, then updated $\mathbf{W}_n$ with the latest $\mathbf{m}$, and repeated this process until the model update fell below the tolerance. In other words, the IRLS algorithm included two loops. The inner loop updated the model $\mathbf{m}$ by solving a bound-constrained L_2 norm

minimization problem, while the outer loop updated the variable weighting matrix $\mathbf{W}_n$. Interested readers can find a detailed description of the minimization process in [37,44].

3. Results

3.1. Synthetic Data Examples

To illustrate the effectiveness of the gravity inversion with different model norms on exploration potential estimation, we present the results of their application to synthetic gravity data produced by a two-block model shown in Figure 4a. Two blocks are parallelepipeds of dimensions 100 × 100 × 100 m, situated at 50 and 100 m depths. The densities of the southwest and northeast blocks are 1 g/cm^3 and 1.5 g/cm^3, respectively. The gravity data caused by two blocks are simulated at equidistant stations laterally spaced at 20 m with a height of 1 m, shown in Figure 4b. All data are contaminated with 2% Gaussian noise to simulate the real scenario.

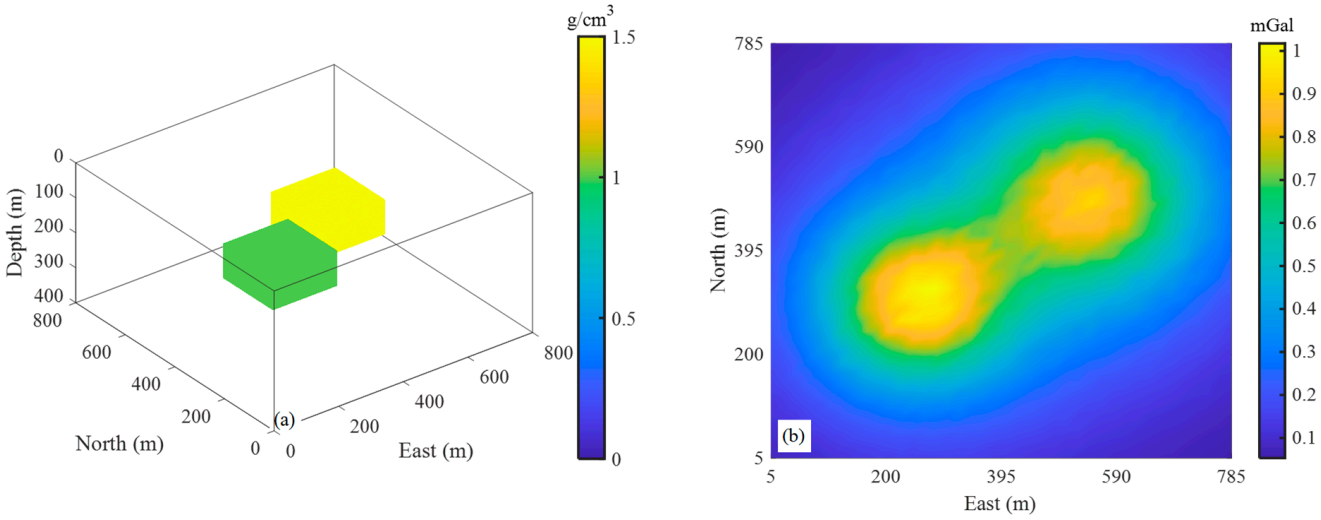

Figure 4. (**a**) A 3D view of the true density model for the first synthetic data example. (**b**) Gravity data produced by the model in (a), 2% Gaussian noise is added.

We have inverted the synthetic data using the L_0, L_1, and L_2 model norms, as introduced in the previous section. The inversion domain is discretized into rectangular cells with a horizontal cell size of 20 × 20 m and a vertical size of 20 m for a total cell count of 32,000. The inversions of three model norms are constrained within the bound of 0–1.5 g/cm^3. All of the inversions were successfully terminated when the data misfit was decreased to the tolerance. Horizontal and vertical sections of the true and inverted models are presented in Figure 5.

It was found that the L_2 norm-based inversion tended to produce a smooth model (Figure 5d–f), which can only roughly show the locations of the density bodies; however, the geometries and edges of the density bodies are very far from the ground truth (Figure 5a–c). The inversion result using the L_1 norm penalty provides a reasonable model with an improved delineation of the geometries yet has fuzzy edges (Figure 5g–i). In contrast, the L_0 norm-based inversion generates a blocky model that clearly defines the density bodies' locations and geometries (Figure 5j–l). The predicted gravity anomalies from the inverted models with three model norms are displayed in Figure 6, which all match the observed gravity anomalies at similar levels. We also found that the L_2 norm-based inversion takes the least time compared to other inversions (Table 1). Furthermore, we performed exploration potential estimations using the inverted models (Table 1). Concerning the L_2 norm-based inversion model, a cutoff value of 0.2 g/cm^3 was used to approximate the geometries of the density bodies. Compared to the theoretical mass of 1.0 × 10^7 tons, the L_0 norm-based inversion provided the closest estimation.

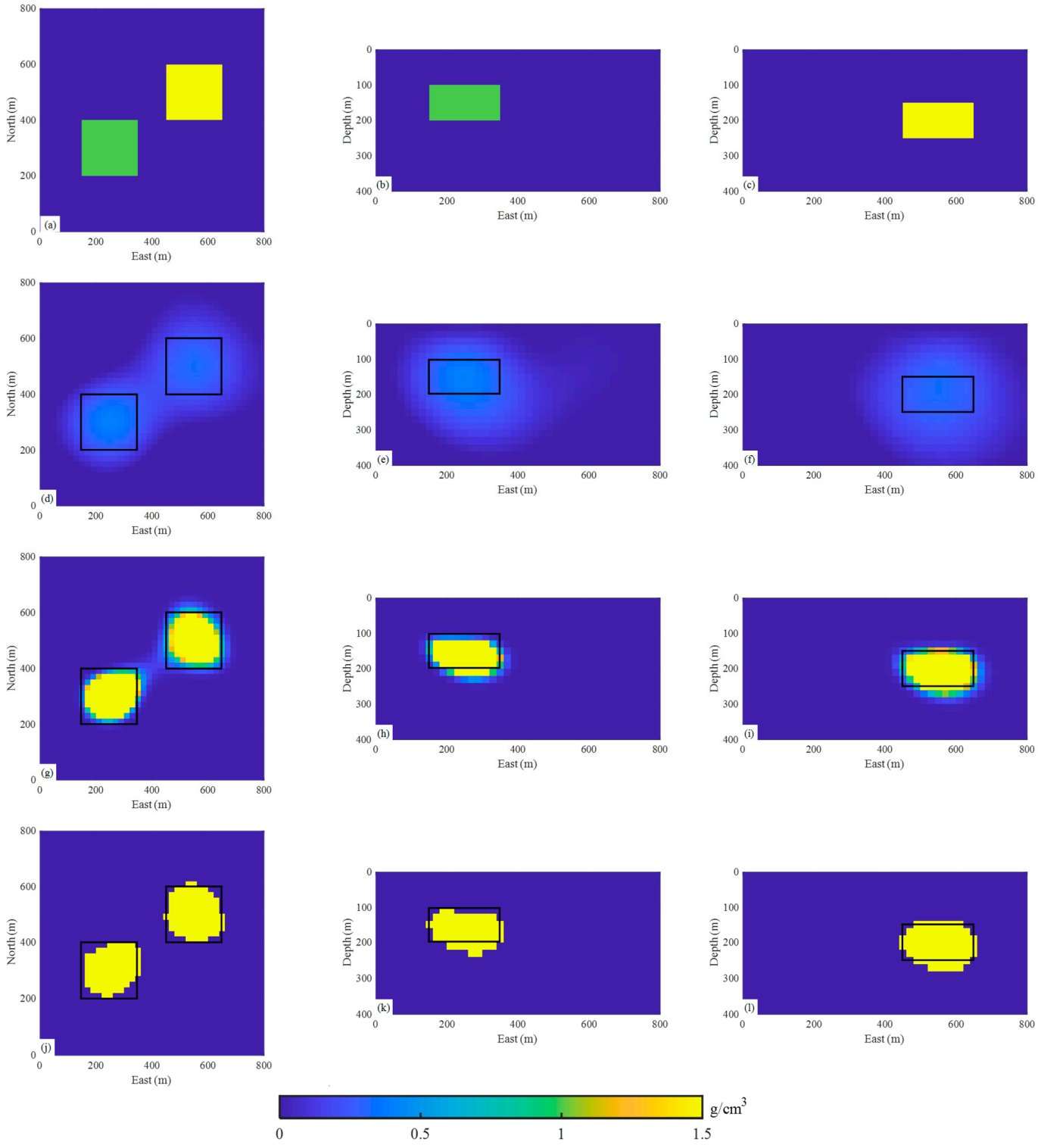

Figure 5. Inversion results of the first synthetic data. (**a**,**d**,**g**,**j**) present horizontal sections at a depth of 160 m. (**b**,**e**,**h**,**k**) present vertical sections at the north of 300 m. (**c**,**f**,**i**,**l**) present vertical sections at the north of 500 m. The first row is the true model. The second to fourth rows give the inverted models using the L_2, L_1, and L_0 norms. The black boxes indicate the location of the true models.

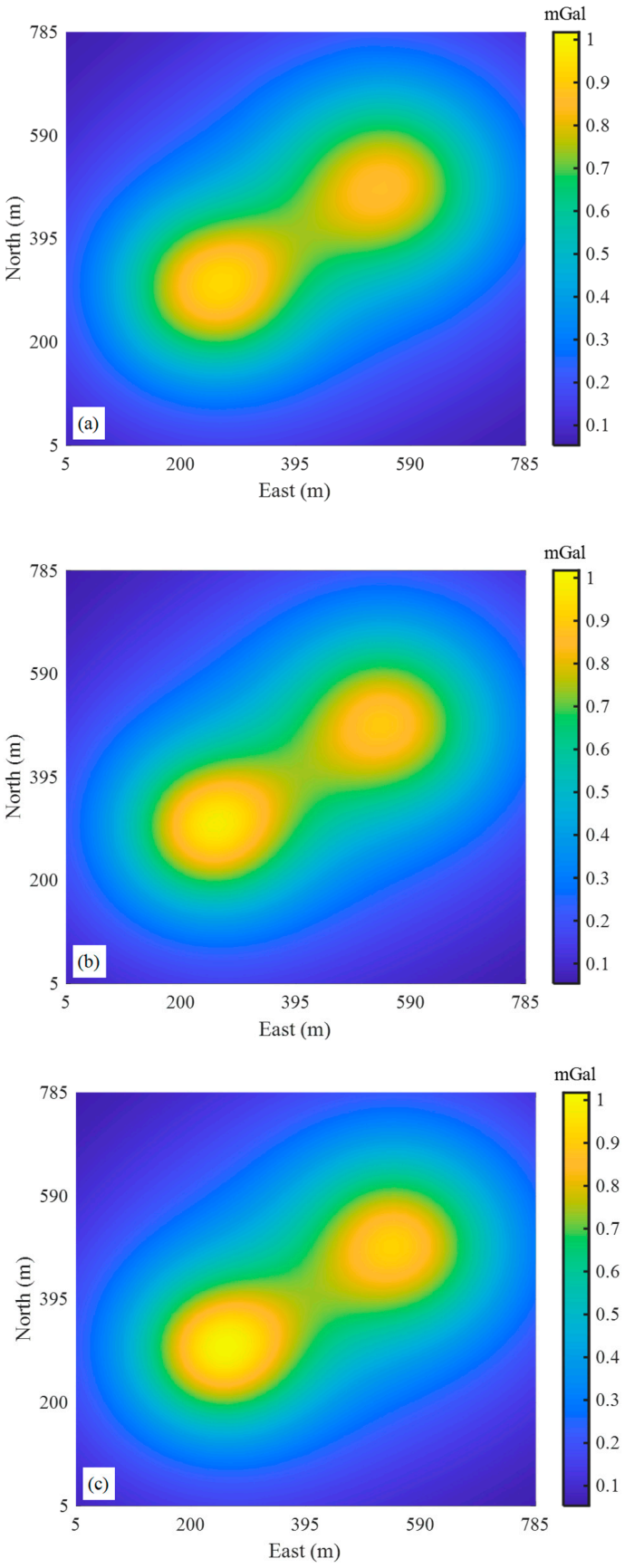

Figure 6. Predicted gravity anomalies of the first synthetic data from the inverted models using the (**a**) L_2, (**b**) L_1, and (**c**) L_0 norm penalties.

Table 1. Summary of the inversion for synthetic data I. The second column presents the predicted noise level (standard deviation) from the recovered models.

Model Norm	Noise Level (mGal)	Time (s)	Exploration Potential (tons)
L_2	1.10×10^{-2}	139	5.20×10^7
L_1	6.00×10^{-3}	512	1.71×10^7
L_0	5.20×10^{-3}	431	1.01×10^7

Another synthetic test was performed to explore the ability of the inversion with different norm penalties to reconstruct more complex structures and estimate the exploration potential of the interested target. Figure 7 demonstrates the perspective view of this model that comprises four density bodies and the gravity anomalies produced by the model with 2% Gaussian noise added. The survey setup, inversion domain, and model discretization are the same as the previous synthetic data test. The inversions of three model norms are constrained within the bound of –1 to 2 g/cm^3.

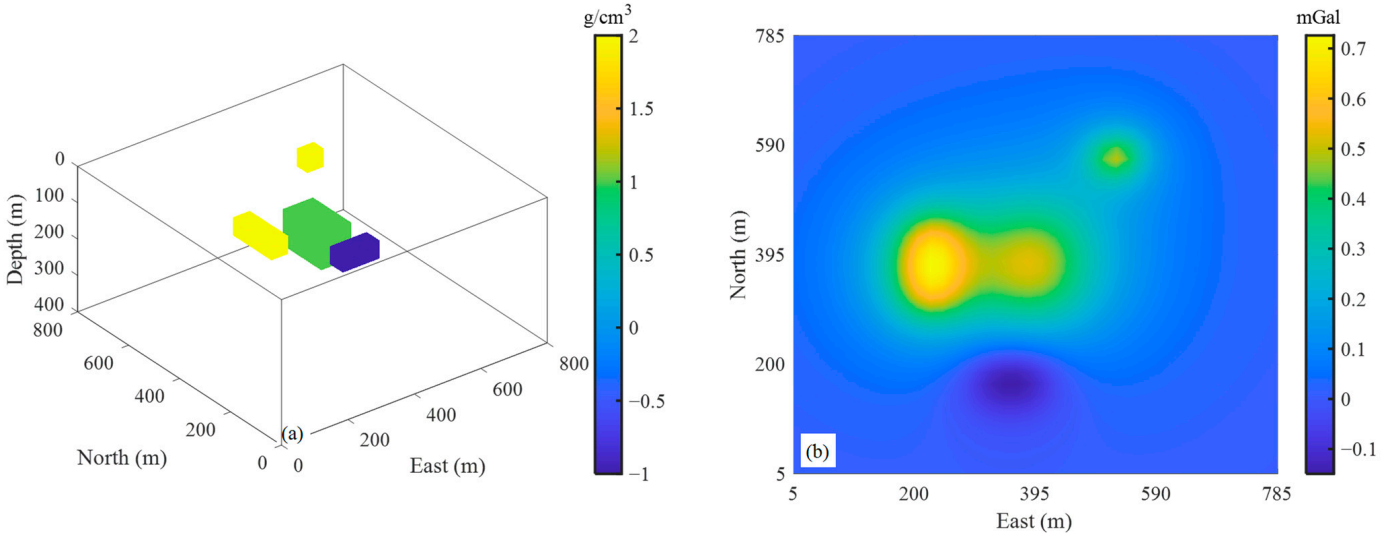

Figure 7. (**a**) Perspective view of the complex model comprises four density bodies. (**b**) Gravity anomalies produced by the model in (**a**), 2% Gaussian noise is added.

The recovered models and corresponding predicted gravity anomalies are displayed in Figures 8 and 9, respectively. All of the inversions fit the observed gravity anomalies at similar noise levels regarding data misfit. When the L_2 norm is concerned, the recovered model is too blurred, and the density bodies are poorly modeled, especially at a deeper depth (Figure 8f). For the L_1 and L_0 norm penalties, the recovered models are featured by sharp boundaries, and the density body located at deeper depth is observed. However, inversion with an L_0 norm penalty provides a fully compact model for shallow and deep density bodies; further, L_0 norm-based inversion result has minimal redundant structures compared to other inversions' results.

Exploration potentials are estimated based on the inversion results resulting from different model norm penalties (Table 2). For this case, we assume that the ore deposits correspond to the positive density bodies. A cutoff value of 0.2 g/cm^3 is used for the L_2 norm-based inversion result to approximate the geometries of the ore deposits. As expected, the L_0 norm-based inversion yields a reliable estimation comparable to the theoretical mass of 2.30×10^6 tons.

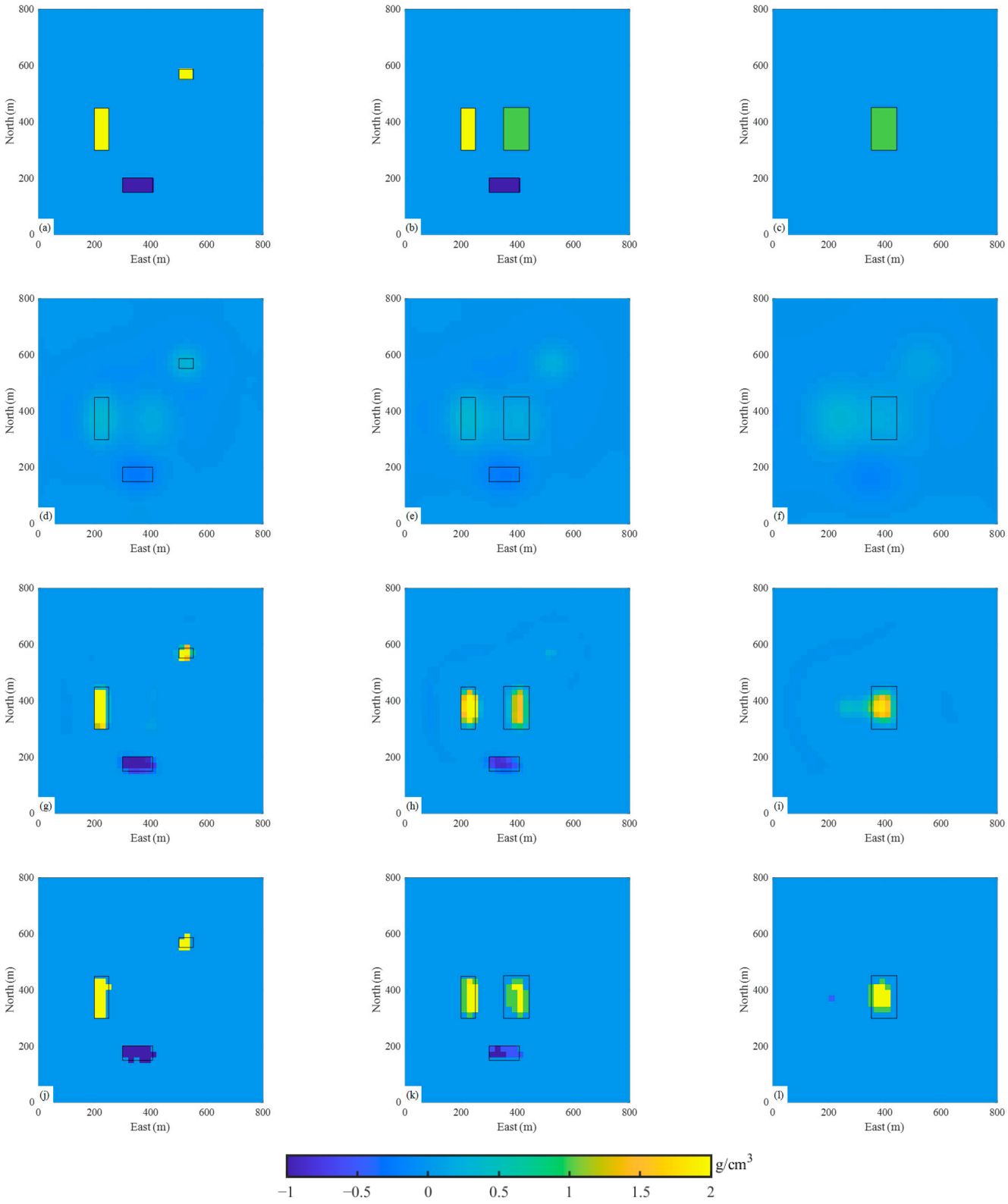

Figure 8. Inversion results of the second synthetic data. (**a**,**d**,**g**,**j**) present horizontal sections at a depth of 60 m. (**b**,**e**,**h**,**k**) present horizontal sections at a depth of 90 m. (**c**,**f**,**i**,**l**) present horizontal sections at a depth of 150 m. The first row is the true model. The second to fourth rows give the inverted models using the L_2, L_1, and L_0 norms. The black boxes indicate the location of the true models.

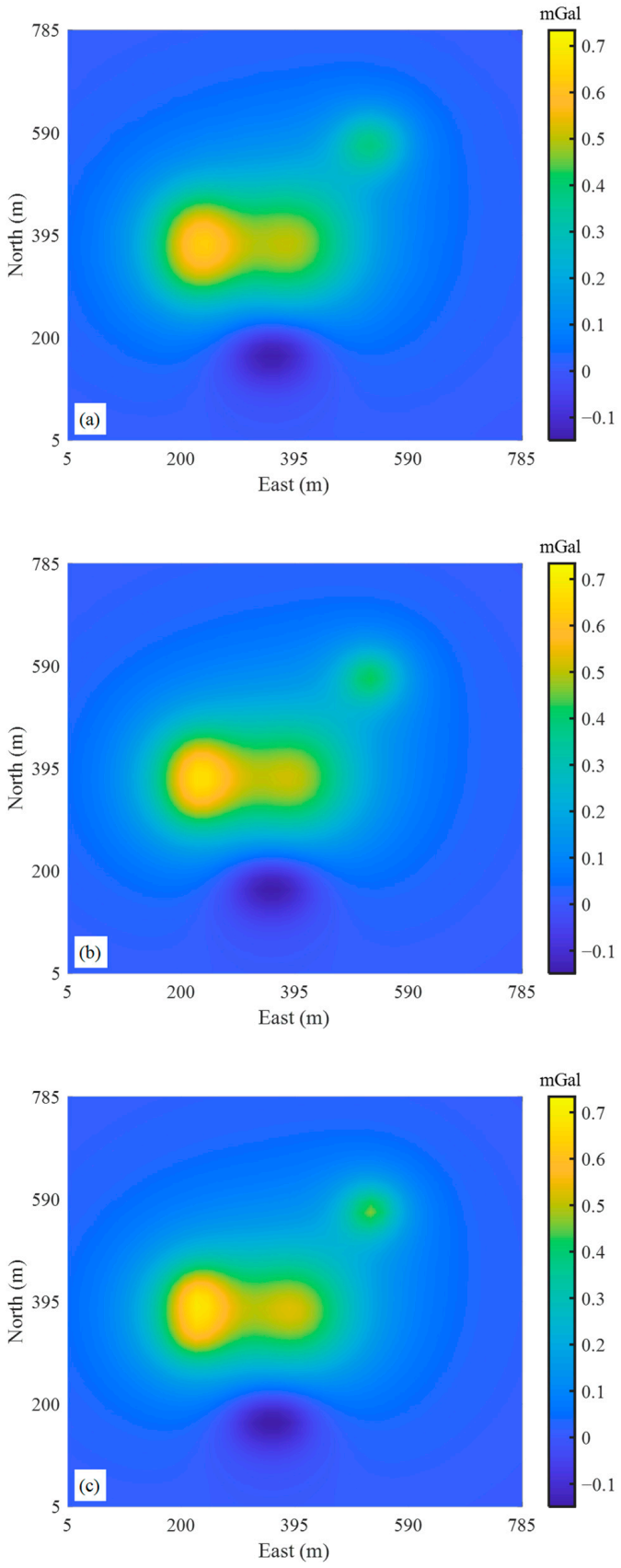

Figure 9. Predicted gravity anomalies of the second synthetic data from the inverted models using the (**a**) L_2, (**b**) L_1, and (**c**) L_0 norm penalties.

Table 2. Summary of the inversion for synthetic data II. The second column presents the predicted noise level (standard deviation) from the recovered models.

Model Norm.	Noise Level (mGal)	Time (s)	Exploration Potential (tons)
L_2	1.03×10^{-2}	106	5.57×10^6
L_1	7.30×10^{-3}	412	5.36×10^6
L_0	5.50×10^{-3}	549	2.32×10^6

3.2. Real Data Application

In this section, the gravity data of the Dida iron ore deposit is employed to verify the applicability of inversion with different norm penalties (Figure 10). The study area is small skarn-type magnetite, and gravity exploration is carried out to expand exploration potential. The tectonic trend of the study area is NNE, which is consistent with the neocathaysian structural system. The ultrabasic rock belt is located in the Late Paleozoic fold belt and consists of sixteen large and small plutons. The plutons are intruded into the Silurian-Devonian Erdaogou group monoclinic stratum controlled by the vertical thrust fault, and it is banded. The plutons have the same trend as the surrounding rock, but the inclination is the opposite [48].

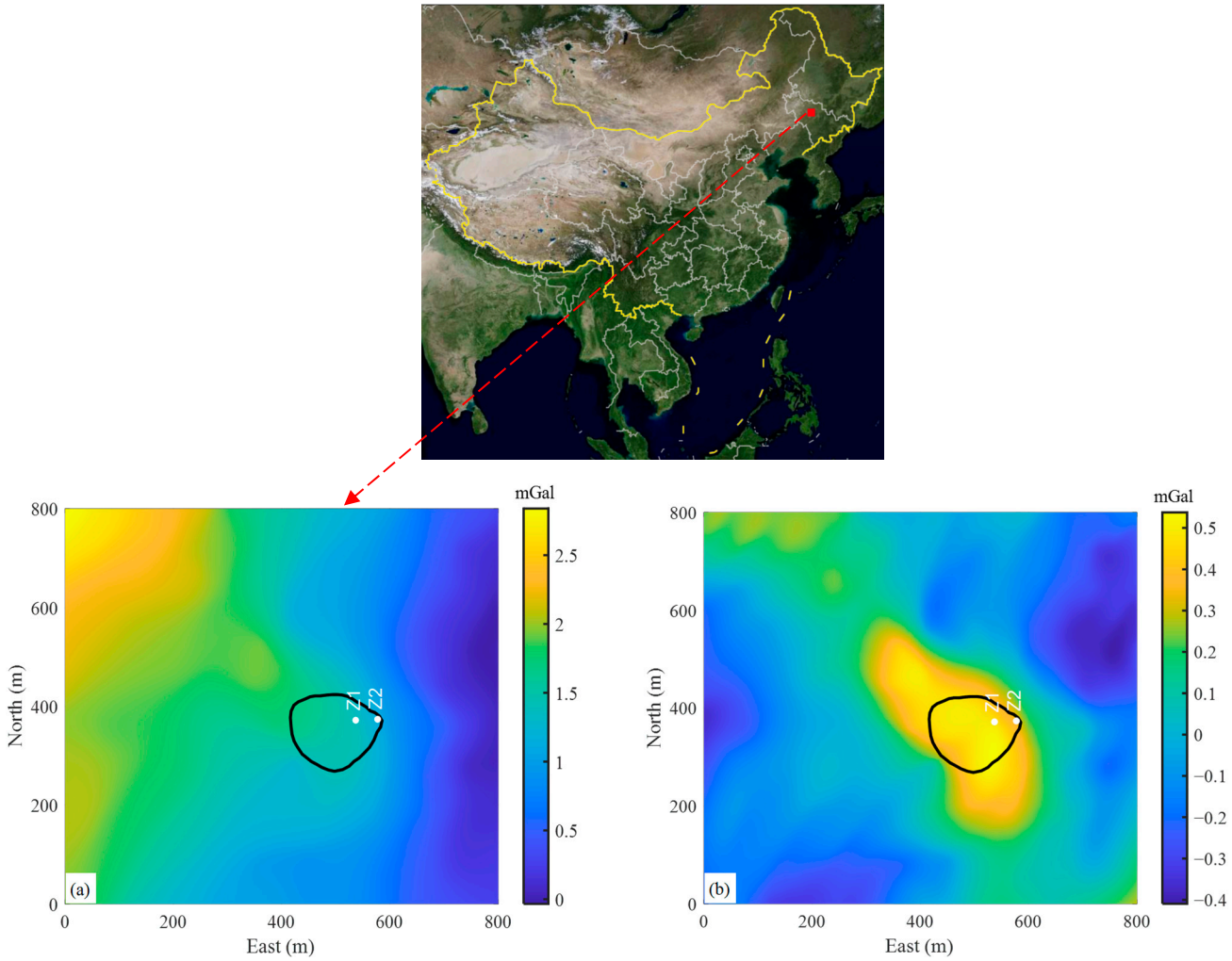

Figure 10. (**a**) The Bouguer gravity anomalies in the Dida ore deposit. (**b**) Residual gravity anomalies. The area enclosed by the solid black line presents the horizontal extent of the ore deposit inferred from drilling results. The white dots show the drilling locations.

The raw gravity data were obtained in the 1970s by measuring at the surface using a quartz spring gravimeter [48]. The available data were archived as the Bouguer gravity data set that has previously been used to test the field separation [49,50]. The Bouguer gravity anomalies (Figure 10a) are digitized carefully from Figure 6 in [49]. The digitization is fulfilled using the open-source software GeoGoku [51]. The digitizing function takes the picture as input, reads contour lines interactively, and finally outputs scatter coordinates and corresponding values. In the process of reading the contour line, one needs to set the value corresponding to the contour line and then manually click the position of the contour line. Then the program will automatically recognize its position and record it. After digitization, the scattered data are re-gridded into 41 × 41 data points with a spacing of 20 m using a Taylor series expansion-based interpolator [52]. We use trend analysis to remove the regional anomalies from the Bouguer gravity anomalies. The first-order trend surface is used to characterize the regional anomalies by trial and error. The corresponding residual gravity anomalies are calculated by subtracting regional anomalies from Bouguer gravity anomalies, presented in Figure 10b. As expected, the iron-caused anomalies are highlighted. Gravity, magnetic interpretation, and drilling results show that the northwest ore body has high magnetization and density relative to the surrounding rock (Figure 10b, northwest of the enclosed black line). In contrast, the southeast ore body (enclosed black line) has low magnetization and high density relative to the surrounding rock [48,53]. From the knowledge of the drilling, the Z2 drilling finds no ore deposit, while the Z1 drilling reveals an iron orebody and its extent up to ~200 m deep [48].

In the inversion phase, we discrete the subsurface of the study area into 100 × 100 × 40 rectangular cells with a spacing of 10 m. The inversion domain is extended by 100 m horizontally to reduce the boundary effects. The bound constraint of the recovered model is determined based on the measurements of the rock samples and is set to –1 to 1.2 g/cm^3 [48]. The noise's uncertainty is set to 5% data magnitude plus a floor of 1×10^{-3} mGal. The recovered models from the inversions based on L_2, L_1, and L_0 norms are displayed in Figure 11, and their predictions of the residual gravity anomalies are shown in Figure 12.

Unsurprisingly, the L_2 norm-based inversion result is rather smooth and provides limited information about the target iron ore deposits. Compared to the L_2 norm inversion, the L_1 and L_0 norm-based inversion results present non-smooth and blocky features. The recovered model is positively correlated with drilling information. In terms of the L_0 norm-based inversion, the geometry and location of the ore deposit are clearly recovered. The exploration target is located in the center of the study area. The horizontal plane shows that the possible extent of the iron ore deposits (Figure 11f) is smaller than that inferred from the drillings (Figure 10b). Further, the vertical section (Figure 11c) shows that the iron ore at the Z1 starts from a depth of 100 m and ends at about 200 m. Compared with the drilling results [48], the estimated top interface of the ore body is shallowly buried. These mismatches are mainly affected by factors such as the accuracy of field separation, the influence of coherent noise in the field data [39], and the bias of the upper and lower bounds of the model parameters caused by the measurement error of the rock samples.

The predicted gravity anomalies (Figure 12) from three inverted models are highly consistent with the input residual gravity anomalies in Figure 10b, demonstrating that the inversions are well solved. We also note that the inversion with the L_2 norm takes the shortest time consumption (271 s), while the L_1 (802 s) and L_0 (2153 s) norm-equipped inversions need more time to converge for searching a compact model.

Finally, we perform the exploration potential estimation based on recovered models with different norms. Since the interested ore bodies are located in the center of the study area, we cropped the inverted models to 100–600 m in the north, 300–700 m in the east, and 80–200 m in depth. Concerning L_2 norm-based inversion, a cutoff value of 0.15 g/cm^3 is applied to the recovered model to approximate the exploration target. There are 6166 cells with a density greater than or equal to 0.15 g/cm^3. Here, we employ the average density of the rock samples (3.67 g/cm^3), and it yields an exploration potential of 7,339,200 tons. Regarding L_1 and L_0 norm-based inversions, their estimations are

6,345,600 and 3,153,600 tons, respectively. It is found in the synthetic data tests that the L_2 or L_1 norm-based inversion tends to overestimate the exploration potential, so it is expected that the exploration potential of the iron ore deposit in Dida is about 3.2 million tons.

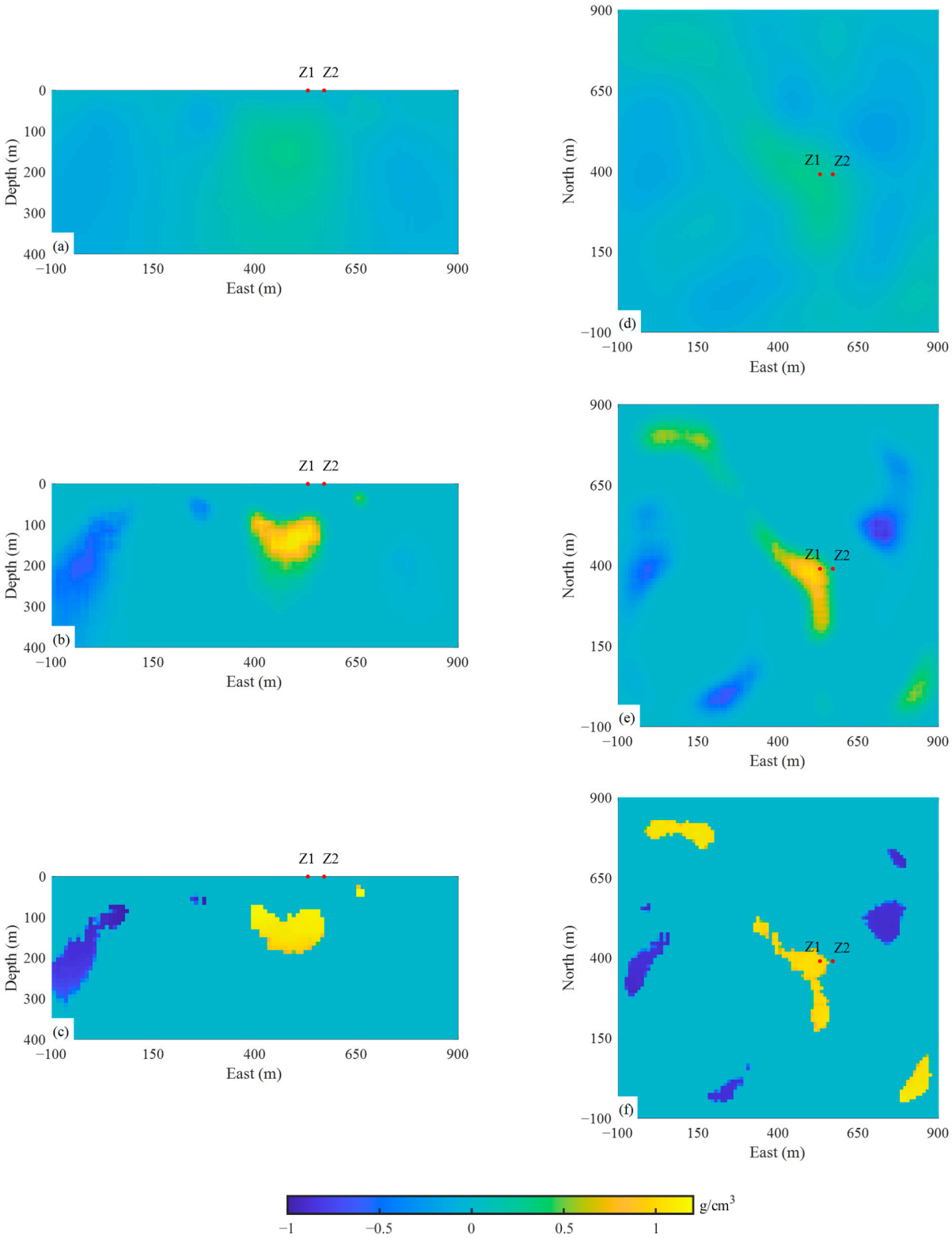

Figure 11. Inversion results of the Dida gravity anomalies. (**a**–**c**) present the vertical sections at north 390 m. (**d**–**f**) show the planes at a depth of 160 m. The first to third rows give the inverted models using the L_2, L_1, and L_0 norms. The red dots represent the drilling locations.

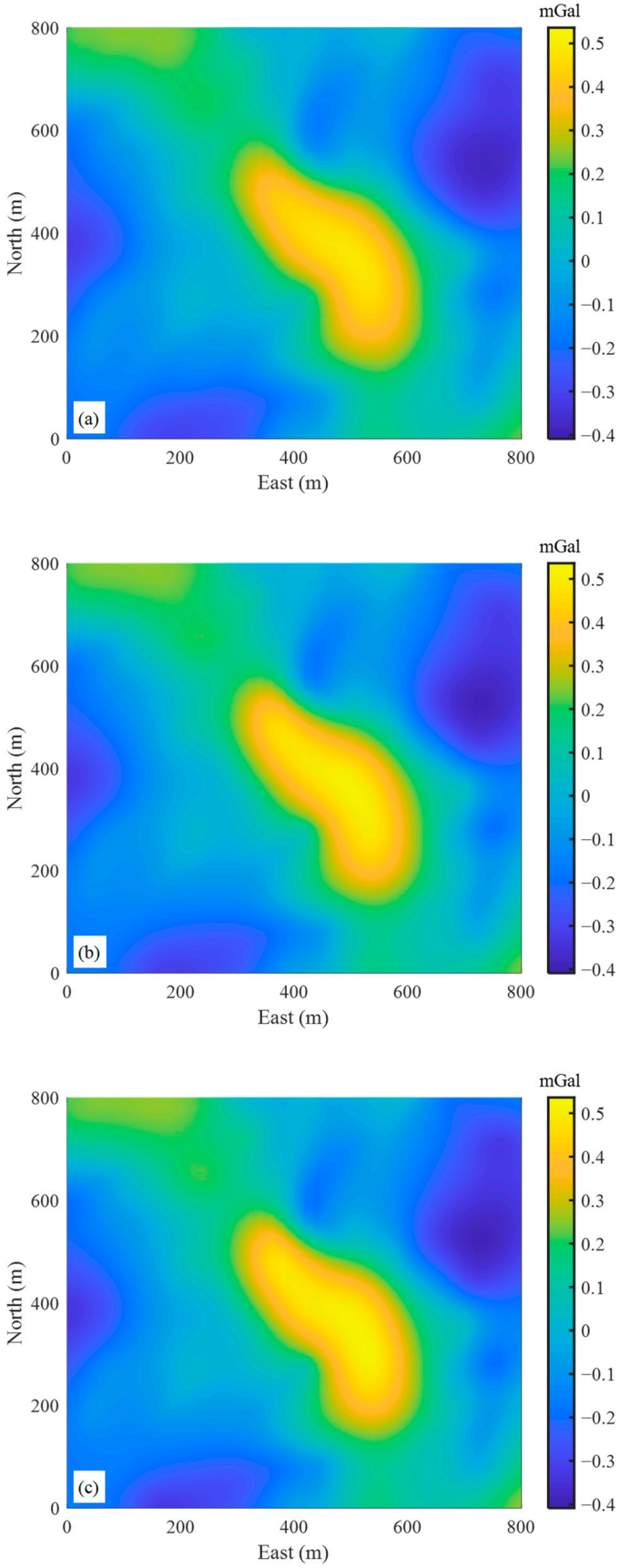

Figure 12. Predictions of the field gravity anomalies from the inverted models using the (**a**) L_2, (**b**) L_1, and (**c**) L_0 norm penalties.

4. Discussion

Exploration potential estimation is crucial in the early stage of mineral exploration and development. However, the currently popular methods all rely on in-situ petrophysical parameters from geological mapping or drilling projects, which are costly and resource-intensive. They are challenging to carry out in large-scale areas. In contrast, geophysical inversion provides an efficient and economical method for estimating exploration potential, which can be used in large mining areas and has great application prospects. The authors of [13] used inversion results from aeromagnetic data to estimate the exploration potential of deep deposits, yet they only used inversion based on the L_2 model norm penalty. Nonetheless, their results reveal the value of inversion-based exploration potential prediction techniques.

Although inversion with different norm penalties has caused a research boom in recent years, however, to our knowledge, studies based on other norms-based inversions in exploration potential estimation have not been reported. This contribution shows the practical value of inversion results of different norms (including the classical L_2 model constraints and the recently popular L_1 and L_0 norm constraints) for exploration potential estimation. We approximate the L_1 and L_0 norms with equivalent formulations, which allow us to evaluate the merits of multiple norms in a numerically feasible way. We added a boundary constraint, commonly used for most geophysical inversions, into the inversion to constrain the recovered model. Benefiting from the characteristic of the L_0 norm penalty, that is, minimizing the number of non-zero model parameters regardless of their magnitude, we found that the L_0 norm-based inversion can better reconstruct the subsurface density structure than other norms. Ultimately, the exploration potentials estimated from L_0 norm-based inversion result also have the slightest deviation compared to the theoretical mass.

This paper compares the applicability of inversion equipped with different norm penalties in exploration potential estimation. However, there are still some issues that need further in-depth research. One valuable research point is to assess the impact of inexact boundary constraints of the inversion on exploration potential estimation. Inexact boundary information is inevitable because the actual measured petrophysical properties (e.g., density) from rock samples are not fixed values but vary within an interval, which presents challenges in setting appropriate upper and lower bounds in the inversion stage. Another research point is the inevitable coherent noise in the data for inversion. In our research experience, this type of noise is often difficult to handle, unlike random noise [34]. Coherent noise may be caused by various factors such as observation error, simulation error, and data processing error. Our future research will focus on these issues.

5. Conclusions

Inversion plays a crucial role in the quantitative interpretation of gravity data. Regardless of the prior information, the model norm penalty in the object function largely determines the interpretability of the recovered model. This paper presents a comparison of inversions with different norm penalties and their applications in the exploration of potential estimation in mineral exploration. Regarding the inversion, depth weighting and cell volume weighting are incorporated into all kinds of norm penalties. Furthermore, a commonly used bound constraint is introduced into the inversions to reduce the ambiguity of the inversion. The L_1 and L_0 norm-based inversions are solved using an IRLS technique. We test the applicability of the different model norms with respect to the fidelity of the inverted model, and we evaluate the performance of the inverted models with different norms for the exploration potential estimation, which is of increasing interest in mineral exploration.

Synthetic data tests and real data applications demonstrate that the inversion equipped with the L_2 norm leads to the generation of a smooth featured model that is difficult to interpret. The L_1 norm penalty can yield a sparse model recovery and improve the interpretability. However, a more compact model characterized by clear boundaries and

minimal redundant structure is preferred to clarify the deeper situated structures' geometries and provide a geologically acceptable model. By our tests, the L_0 norm equipped inversion shows evident merit in estimating the exploration potential.

Author Contributions: Conceptualization, T.C.; methodology, T.C.; validation, T.C.; investigation and visualization, T.C.; writing—original draft preparation, T.C.; writing—review and editing, T.C. and G.Z.; supervision, G.Z.; project administration, G.Z. All authors have read and agreed to the published version of the manuscript.

Funding: This research was funded in part by the Stable-Support Scientific Project of China Research Institute of Radiowave Propagation (A132007W06), in part by the National Natural Science Foundation of China (41630320), and in part by the Terrestrial and Oceanic Geological Map Updating and Sharing Program of China (DD20190370).

Data Availability Statement: The synthetic data underlying this article will be shared upon reasonable request to the corresponding author.

Acknowledgments: The authors thank Zelin Li (Hebei University of Engineering) for his discussion and help with the inversion implementation.

Conflicts of Interest: The authors declare no conflict of interest.

References

1. Wang, G.; Huang, L. 3D geological modeling for mineral resource assessment of the Tongshan Cu deposit, Heilongjiang Province, China. *Geosci. Front.* **2012**, *3*, 483–491. [CrossRef]
2. Mery, N.; Emery, X.; Cáceres, A.; Ribeiro, D.; Cunha, E. Geostatistical modeling of the geological uncertainty in an iron ore deposit. *Ore Geol. Rev.* **2017**, *88*, 336–351. [CrossRef]
3. Silva, D.; Almeida, J. Geostatistical methodology to characterize volcanogenic massive and stockwork ore deposits. *Minerals* **2017**, *7*, 238. [CrossRef]
4. Lamamra, A.; Neguritsa, D.L.; Mazari, M. Geostatistical modeling by the Ordinary Kriging in the estimation of mineral resources on the Kieselguhr mine, Algeria. *IOP Conf. Ser. Earth Environ. Sci.* **2019**, *362*, 012051. [CrossRef]
5. Matheron, G. Principles of geostatistics. *Econ. Geol.* **1963**, *58*, 1246–1266. [CrossRef]
6. Zhu, Z.X.; Yan, J.D. The application of SD method in mineral resources reserves calculation in the Jiguanzi Copper-gold deposit, Daye, Hubei province. *Geol. Explor.* **2004**, *40*, 82.
7. Battalgazy, N.; Madani, N. Categorization of mineral resources based on different geostatistical simulation algorithms: A case study from an iron ore deposit. *Nat. Resour. Res.* **2019**, *28*, 1329–1351. [CrossRef]
8. Truong, X.L.; Truong, X.Q.; Nguyen, T.A.; Raghavan, V.; Nguyen, C.C. Development of HUMGEOSTAT: A new geological tool for geostatistical analysis of mineral deposit: A case study at sin Quyen mine (northern Vietnam). *J. Geol. Soc. India* **2019**, *93*, 574–582. [CrossRef]
9. Wellmer, F.W.; Dalheimer, M.; Wagner, M. *Economic Evaluations in Exploration*, 2nd ed.; Springer Science & Business Media: Berlin, Germany, 2007.
10. Erarslan, K. Computer aided ore body modelling and mine valuation. *Earth Sci.* **2012**, *16*, 345–372.
11. Onur, A.H.; Konak, G.; Karakuş, D. Limestone quarry quality optimization for a cement factory in Turkey. *J. South. Afr. Inst. Min. Metall.* **2008**, *108*, 751–757.
12. Xu, S.; Sirieix, C.; Marache, A.; Riss, J.; Malaurent, P. 3D geostatistical modeling of Lascaux hill from ERT data. *Eng. Geol.* **2016**, *213*, 169–178. [CrossRef]
13. Gao, X.; Xiong, S.; Yu, C.; Zhang, D.; Wu, C. The Estimation of Magnetite Prospective Resources Based on Aeromagnetic Data: A Case Study of Qihe Area, Shandong Province, China. *Remote Sens.* **2021**, *13*, 1216. [CrossRef]
14. Li, Y.; Oldenburg, D.W. 3-D inversion of magnetic data. *Geophysics* **1996**, *61*, 394–408. [CrossRef]
15. Li, Y.; Oldenburg, D.W. 3-D inversion of gravity data. *Geophysics* **1998**, *63*, 109–119. [CrossRef]
16. Meng, Z. Three-dimensional potential field data inversion with L0 quasinorm sparse constraints. *Geophys. Prospect.* **2018**, *66*, 626–646. [CrossRef]
17. Sun, Y.; Schaefer, S.; Wang, W. Denoising point sets via L0 minimization. *Comput. Aided Geom. Des.* **2015**, *35*, 2–15. [CrossRef]
18. Hyder, M.; Mahata, K. An approximate l0 norm minimization algorithm for compressed sensing. In Proceedings of the 2009 IEEE International Conference on Acoustics, Speech and Signal Processing, Taipei, China, 19–24 April 2009; pp. 3365–3368.
19. Sun, Y.; Tao, J. Image reconstruction from few views by $\ell 0$-norm optimization. *Chin. Phys. B* **2014**, *23*, 078703. [CrossRef]
20. Fan, Z.; Ni, M.; Zhu, Q.; Sun, C.; Kang, L. L0-norm sparse representation based on modified genetic algorithm for face recognition. *J. Vis. Commun. Image Represent.* **2015**, *28*, 15–20. [CrossRef]
21. Wang, S.; Wu, W.; Feng, J.; Liu, F.; Yu, H. Low-dose spectral CT reconstruction based on image-gradient L0-norm and adaptive spectral PICCS. *Phys. Med. Biol.* **2020**, *65*, 245005. [CrossRef]

22. Chen, G.; Chen, S.; Wang, H.; Zhang, B. Geophysical data sparse reconstruction based on L0-norm minimization. *Appl. Geophys.* **2013**, *10*, 181–190. [CrossRef]
23. Zhong, S.; Wang, Y.; Zheng, Y.; Wu, S.; Chang, X.; Zhu, W. Electrical resistivity tomography with smooth sparse regularization. *Geophys. Prospect.* **2021**, *69*, 1773–1789. [CrossRef]
24. Yang, J.; Yin, C.; Dai, R.; Yang, S.; Zhang, F. Seismic impedance inversion via L0 gradient minimisation. *Explor. Geophys.* **2019**, *50*, 575–582. [CrossRef]
25. Last, B.; Kubik, K. Compact gravity inversion. *Geophysics* **1983**, *48*, 713–721. [CrossRef]
26. Portniaguine, O.; Zhdanov, M. Focusing geophysical inversion images. *Geophysics* **1999**, *64*, 874–887. [CrossRef]
27. Ghalehnoee, M.; Ansari, A.; Ghorbani, A. Improving compact gravity inversion based on new weighting functions. *Geophys. J. Int.* **2016**, *208*, 546–560. [CrossRef]
28. Meng, Z.; Xu, X.; Huang, D. Three-dimensional gravity inversion based on sparse recovery iteration using approximate zero norm. *Appl. Geophys.* **2018**, *15*, 524–535. [CrossRef]
29. Tibshirani, R. Regression shrinkage and selection via the lasso. *J. R. Stat. Soc. Ser. B (Methodol.)* **1996**, *58*, 267–288. [CrossRef]
30. Utsugi, M. Magnetic inversion to recover the subsurface block structures based on L1 norm and total variation regularization. *Geophys. J. Int.* **2022**, *228*, 510–537. [CrossRef]
31. Nagy, D. The gravitational attraction of a right rectangular prism. *Geophysics* **1966**, *31*, 362–371. [CrossRef]
32. Talwani, M.; Ewing, M. Rapid computation of gravitational attraction of three-dimensional bodies of arbitrary shape. *Geophysics* **1960**, *25*, 203–225. [CrossRef]
33. Paul, M.K. The gravity effect of a homogeneous polyhedron for three-dimensional interpretation. *Pure Appl. Geophys.* **1974**, *112*, 553–561. [CrossRef]
34. Okabe, M. Analytical expressions for gravity anomalies due to homogeneous polyhedral bodies and translations into magnetic anomalies. *Geophysics* **1979**, *44*, 730–741. [CrossRef]
35. Haáz, I.B. Relations between the potential of the attraction of the mass contained in a finite rectangular prism and its first and second derivatives. *Geophys. Trans. II* **1953**, *7*, 57–66.
36. Li, X.; Chouteau, M. Three-dimensional gravity modeling in all space. *Surv. Geophys.* **1998**, *19*, 339–368. [CrossRef]
37. Holland, P.W.; Welsch, R.E. Robust regression using iteratively reweighted least-squares. *Commun. Stat.-Theory Methods* **1977**, *6*, 813–827. [CrossRef]
38. Chen, T.; Zhang, G. Forward modeling of gravity anomalies based on cell mergence and parallel computing. *Comput. Geosci.* **2018**, *120*, 1–9. [CrossRef]
39. Chen, T.; Yang, D. Modeling and Inversion of Airborne and Semi-Airborne Transient Electromagnetic Data with Inexact Transmitter and Receiver Geometries. *Remote Sens.* **2022**, *14*, 915. [CrossRef]
40. Portniaguine, O.; Zhdanov, M.S. 3-D magnetic inversion with data compression and image focusing. *Geophysics* **2002**, *67*, 1532–1541. [CrossRef]
41. Hanke, M. Limitations of the L-curve method in ill-posed problems. *BIT Numer. Math.* **1996**, *36*, 287–301. [CrossRef]
42. Golub, G.H.; Heath, M.; Wahba, G. Generalized cross-validation as a method for choosing a good ridge parameter. *Technometrics* **1979**, *21*, 215–223. [CrossRef]
43. Grayver, A.V.; Streich, R.; Ritter, O. Three-dimensional parallel distributed inversion of CSEM data using a direct forward solver. *Geophys. J. Int.* **2013**, *193*, 1432–1446. [CrossRef]
44. Li, Z.; Yao, C.; Zheng, Y.; Wang, J.; Zhang, Y. 3D magnetic sparse inversion using an interior-point method. *Geophysics* **2018**, *83*, J15–J32. [CrossRef]
45. Rao, B.D.; Kreutz-Delgado, K. An affine scaling methodology for best basis selection. *IEEE Trans. Signal Process.* **1999**, *47*, 187–200. [CrossRef]
46. Lau, A.; Yin, C. L0 + L1 + L2 mixed optimization: A geometric approach to seismic imaging and inversion using concepts in topology and semigroup. *arXiv* **2010**, arXiv:1007.1880.
47. Li, Y.; Oldenburg, D.W. Fast inversion of large-scale magnetic data using wavelet transforms and a logarithmic barrier method. *Geophys. J. Int.* **2003**, *152*, 251–265. [CrossRef]
48. Chen, S. *Gravity Exploration*, 1st ed.; Geological Publishing House: Beijing, China, 1987; pp. 272–283. (In Chinese)
49. Zeng, H.; Xu, D.; Tan, H. A model study for estimating optimum upward continuation height for gravity separation with application to a Bouguer gravity anomaly over a mineral deposit, Jilin province, northeast China. *Geophysics* **2007**, *72*, I45–I50. [CrossRef]
50. Guo, L.; Meng, X.; Chen, Z.; Li, S.; Zheng, Y. Preferential filtering for gravity anomaly separation. *Comput. Geosci.* **2013**, *51*, 247–254. [CrossRef]
51. GeoGoku. Available online: https://github.com/GeoGoku (accessed on 12 April 2022).
52. Chen, T.; Yang, D. Potential field data interpolation by Taylor series expansion. *Geophysics* **2022**, *87*, G15–G27. [CrossRef]
53. Zeng, H. *Gravity Field and Gravity Exploration*, 1st ed.; Geological Publishing House: Beijing, China, 2005; pp. 251–254. (In Chinese with English Contents)